

First-principles study of LaOPbBiS₃ and its analogous compounds as thermoelectric materials

Keiya Kurematsu¹⁾, Masayuki Ochi¹⁾, Hidetomo Usui²⁾, and Kazuhiko Kuroki¹⁾

¹⁾Department of Physics, Osaka University, Machikaneyama-cho, Toyonaka, Osaka 560-0043, Japan

²⁾Department of Material Science, Shimane University, Matsue, Shimane 690-8504, Japan

(Dated: June 28, 2019)

LaOBiPbS₃ is a kind of pnictogen-dichalcogenide layered compounds, which have recently been experimentally investigated as thermoelectric materials owing to their low thermal conductivity and high controllability of constituent elements. However, thermoelectric performance of LaOBiPbS₃ is at present not very high and that of its analogous compounds remains to be unknown. In this study, we theoretically investigate thermoelectric properties of 24 possible variations of the constituent elements in LaOBiPbS₃ from the viewpoint of the electronic structure. We find that some compounds can have much better thermoelectric performance than LaOBiPbS₃; in particular, LaOSbPbSe₃ is predicted to have a power factor five times as large as that of LaOBiPbS₃. Here, the choice of the pnictogen atom (As, Sb, and Bi), of which the low-energy conduction bands mainly consist, correlates with the calculated power factor and the dimensionless figure of merit, ZT . Such correlation comes from the fact that the low-dimensionality of the electronic structure, which enhances the density of states near the band edge, strongly depends on the pnictogen atom through, e.g., the strength of the spin-orbit coupling. Moreover, hybridization of the wave functions in the pnictogen-dichalcogenide layer and those in the rock-salt layer plays a key role in gap opening, and thus is important for achieving high thermoelectric performance. In LaOSbPbSe₃, such hybridization also pushes up the conduction band bottom, which enhances the density of states near the band edge and thus the power factor.

I. INTRODUCTION

Thermoelectric generation has recently been receiving a lot of attention because of its importance in energy harvesting, and many researchers seek high-performance thermoelectric materials for putting it to partial use. The efficiency of thermoelectric conversion is assessed by the dimensionless figure of merit, ZT :

$$ZT = \frac{\sigma S^2}{\kappa} T = \frac{PF}{\kappa_{el} + \kappa_{ph}} T, \quad (1)$$

where σ , S , κ and T are the electrical conductivity, the Seebeck coefficient, the thermal conductivity, and the temperature, respectively. In the rightmost term of Eq. (1), the thermal conductivity is written as the sum of the electronic and the phononic contribution: $\kappa = \kappa_{el} + \kappa_{ph}$, and the power factor is defined as follows: $PF = \sigma S^2$, which is also used for measuring the thermoelectric performance. Through a long attempt to increase ZT and PF , several favorable aspects of the electronic structure were found, such as the multi-valley band structure¹ and the low-dimensionality²⁻⁵.

From this viewpoint, pnictogen-dichalcogenide layered compounds⁶, such as Bi₄O₄S₃ and $LnOBiS_2$ ($Ln = La, Nd, Ce$, etc.), which have been well-known as a superconductor⁷⁻¹¹ and recently gathered attention also as a thermoelectric material¹², are promising because they possess low-dimensional as well as multi-valley band structure, owing to the quasi-one-dimensional character of the $Pn-p_{x,y}$ orbitals in the conducting $PnCh_2$ layer ($Pn = \text{Pnictogen} = Bi, Sb; Ch = \text{Chalcogen} = S, Se$)¹³⁻¹⁵ alternately stacked with the insulating layer. A rich variety of the insulating layer, such as LnO in $LnOBiS_2$, is also preferable because it offers high controllability of the crystal structure. In addition, it was shown that the rattling motion of the Bi atom possibly reduces the thermal conductivity in

LaOBiS_{2-x}Se_x^{16,17}. As a matter of fact, LaOBiSe was reported to exhibit a relatively high $ZT \sim 0.36$ at 650 K with the low thermal conductivity $\kappa \sim 0.8\text{--}1.2 \text{ W m}^{-1} \text{ K}^{-1}$ ¹⁸. It is noteworthy that a recent theoretical study¹⁴ pointed out that the thermoelectric performance of $LnOBiS_2$ can be sizably enhanced by using lighter and heavier elements for the pnictogen and chalcogen atoms, respectively. Along this line, recent experimental findings are intriguing: $LnOSbSe_2$ exhibits a low thermal conductivity, $1.5 \text{ W m}^{-1} \text{ K}^{-1}$ for $Ln = La$ and $0.8 \text{ W m}^{-1} \text{ K}^{-1}$ for $Ln = Ce$ ¹⁹, and ZT is enhanced by a partial substitution of Sb for Bi in $NdO_{0.8}F_{0.2}BiSe_2$ ²⁰.

Given this background, searching thermoelectric materials with the $PnCh_2$ layer is an attractive idea. One possible candidate is LaOBiPbS₃^{21,22}, where the BiS₂ conducting layer is stacked not only with the LaO insulating layer but also with the PbS rock-salt layer, as shown in Fig. 1. We note that, while Bi and Pb located at the $M1$ and $M2$ sites are not completely ordered, it was shown that the $M1$ ($M2$) site is mainly occupied by Bi (Pb) atom²². From now on, this composition is denoted by LaO(PbS)BiS₂, by which one can easily see the constituent elements of each layer. It is advantageous that the electron carrier doping is possible by a partial replacement of oxygen with fluorine²³. While the thermoelectric performance of LaO(PbS)BiS₂ is at present not very high, e.g., $PF \sim 1.5 \mu\text{W cm}^{-1} \text{ K}^{-2}$ at 770 K²³, a possible enhancement of its performance is expected through a change of the constituent elements because of its large degrees of freedom, most of which still have remained unexplored.

In this study, we theoretically investigate the thermoelectric properties of LaO($TtCh^A$) $PnCh_2^B$ ($Pn = As, Sb, Bi; Tt = \text{Tetrel} = Sn, Pb; Ch^{A,B} = S, Se$). We find a correlation between the choice of the Pn atom, of which the low-energy conduction bands mainly consist, and the calculated PF and ZT . Such correlation comes from the fact that the low-dimensionality of the electronic structure, which enhances the density of states

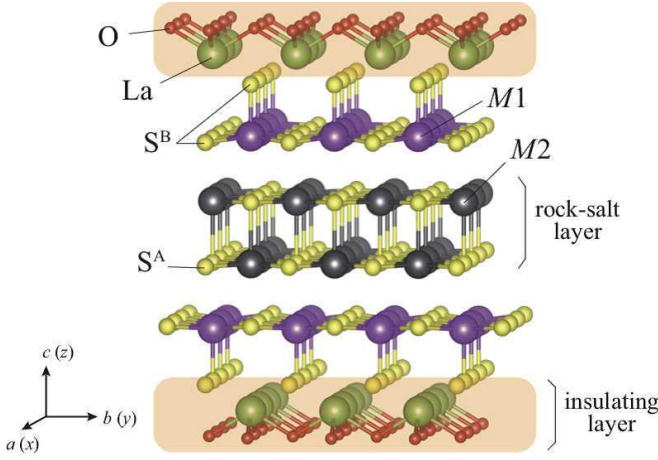


FIG. 1. Crystal structure of $\text{LaO}(\text{PbS})\text{BiS}_2$. In this study, we assumed that the $M1$ and $M2$ sites are occupied by Bi and Pb atoms, respectively (see the main text for detail). Depicted using the VESTA software²⁴.

(DOS) near the band edge, strongly depends on the Pn atom through, e.g., the strength of the spin-orbit coupling (SOC). In addition, hybridization of the wave functions in the $PnCh_2^B$ layer and those in the $TtCh^A$ rock-salt layer plays a key role in gap opening, and thus is important for high thermoelectric performance. A calculated power factor of $\text{LaO}(\text{PbS})\text{BiS}_2$ is enhanced by a factor of five in $\text{LaO}(\text{PbSe})\text{SbSe}_2$, where the hybridization mentioned above also pushes up the conduction band bottom, which enhances DOS near the band edge and thus the power factor.

This paper is organized as follows. Section II presents the detailed procedure of our calculation and a brief description of the Boltzmann transport theory used in our work. We present the basic thermoelectric properties of $\text{LaO}(\text{PbS})\text{BiS}_2$ in Sec. III A. Section III B presents calculated PF and ZT for all the chemical compositions investigated in this study, and theoretical analysis of it to clarify the role of each atom in $\text{LaO}(\text{PbS})\text{BiS}_2$. Section IV is devoted to the conclusion of this study.

II. CALCULATION METHOD

First, we optimized the crystal structure of our target materials using the Perdew-Burke-Ernzerhof exchange-correlation functional revised for solids (PBEsol)²⁵ and the projector-augmented wave method²⁶ as implemented in the *Vienna ab initio simulation package* (VASP)^{27–30}. Our calculation started from the experimental crystal structure of $\text{LaO}(\text{PbS})\text{BiS}_2$ taken from Ref.²², and kept its symmetry, i.e., a space group of $P4/nmm$ and the Wyckoff positions of the atoms therein, during the structural optimization. In addition, we assumed that our target material consists of the LaO , $TtCh^A$, and $PnCh_2^B$ layers, i.e., we neglected the antisite occupation of the Tt and Pn sites. Further detailed analysis of the crystal symmetry and the antisite occupation is an important but challenging future is-

sue. In the structural optimization, we used a $10 \times 10 \times 3$ k mesh and a plane-wave cutoff energy of 550 eV with the inclusion of SOC. Obtained lattice constants for all the materials investigated in this study are shown in Appendix B.

Using the optimized crystal structure, we next performed band-structure calculation using the modified Becke-Johnson potential proposed by Tran and Blaha^{31,32} and the full-potential (linearized) augmented plane-wave method as implemented in the WIEN2K package³³. We used a $16 \times 16 \times 3$ k mesh and set the RK_{max} parameter to 7. SOC was included unless noted. Finally, we calculated the transport properties using the BoltzTraP package³⁴. Using this package, one can calculate the following quantities on the basis of the Boltzmann transport theory with the constant relaxation-time approximation,

$$\sigma = e^2 K_0, \quad S = -\frac{1}{eT} K_0^{-1} K_1, \quad (2)$$

$$\kappa_{\text{el}} = \frac{1}{T} [K_2 - K_1 K_0^{-1} K_1], \quad (3)$$

where $e(>0)$ is the elementary charge and the K_ν is the transport coefficient expressed as follows:

$$K_\nu = \tau \sum_{n,k} v_{n,k} \otimes v_{n,k} \left[-\frac{\partial f_0}{\partial E_{n,k}} \right] (E_{n,k} - \mu(T))^\nu, \quad (4)$$

where τ , $v_{n,k}$, f_0 , $E_{n,k}$, $\mu(T)$ are the relaxation time, the group velocity of the electron on the n -th band at the certain Bloch wave vector k , the Fermi-Dirac distribution function, electronic energy dispersion and the chemical potential, respectively. For calculating these quantities, we used a $62 \times 62 \times 12$ k mesh and the temperature $T = 300$ K. Because an experimental study on $\text{LaO}_{1-x}\text{F}_x(\text{PbS})\text{BiS}_2$ succeeded in performing electron-carrier doping by a partial replacement of oxygen with fluorine²³, we concentrated on the transport properties in the electron-doped region using the rigid-band approximation. In addition, we concentrated on the in-plane diagonal components of these tensors, e.g., $\text{PF} = \text{PF}_{xx} = \text{PF}_{yy}$, because the off-diagonal components vanish for the space group of $P4/nmm$ and the electronic conductivity along the z axis is very small owing to the existence of the insulating layer. Because it is challenging to determine the relaxation time τ and the lattice thermal conductivity κ_{ph} with first-principles calculation, we assumed $\tau = 5.0 \times 10^{-15}$ s and $\kappa_{\text{ph}} = 3.0 \text{ W m}^{-1} \text{ K}^{-1}$ in this study. This value of the relaxation time is typical for thermoelectric materials. The lattice thermal conductivity here was determined by reference to the experimental total thermal conductivity of $\text{LaO}(\text{PbS})\text{BiS}_2$, $\kappa \sim 1\text{--}4 \text{ W m}^{-1} \text{ K}^{-1}$ at 50–300 K²¹.

To obtain the orbital-decomposed band dispersion, we extracted the Wannier functions from the first-principles band structure without the maximal localization procedure by using the WIEN2WANNIER and WANNIER90 packages^{35–38}. We took the p orbitals of all the atoms except for La as the Wannier functions, using a $10 \times 10 \times 3$ k mesh in the Wannier construction. We also used these Wannier functions to see the role of the rock-salt layer in the thermoelectric performance, which we shall describe later in Sec. III B 4. In Sec. III B 4, we also calculated the transport properties using the tight-binding

model consisting of the Wannier functions. For this purpose, we used a $240 \times 240 \times 60$ k -mesh.

III. RESULTS AND DISCUSSION

A. Thermoelectric properties of $\text{LaO}(\text{PbS})\text{BiS}_2$

To begin with, we investigated the electronic structure of $\text{LaO}(\text{PbS})\text{BiS}_2$. Figure 2(a) presents its first-principles band structure calculated with SOC. As shown by first-principles calculation presented in Ref.²², the valence and conduction bands mainly consist of the Bi- p orbitals in the BiS_2 layer and the S- p orbitals in the PbS rock-salt layer, respectively. In other words, the band structure of $\text{LaO}(\text{PbS})\text{BiS}_2$ near the valence-band top can be regarded as a consequence of the hybridization between the conduction bands of the BiS_2 layer and the valence bands of the PbS rock-salt layer. We note that the conduction bands here are quite similar to those in LaOBiS_2 , which has a stacked structure of the LaO insulating layer and the BiS_2 conducting layer¹³. A difference between them, except the hybridization mentioned above, is the existence of the Pb- p band edge in $\text{LaO}(\text{PbS})\text{BiS}_2$, which is indicated by a red dotted arrow (a dotted arrow with a higher energy at the X point) in Fig. 2(a). Another dotted arrow colored in blue (a dotted arrow with a lower energy at the X point) in Fig. 2(a) denotes the band edge of the Bi- p bands. At the $X = (\pi a^{-1}, 0, 0)$ point, the Bi- $p_{x,y}$ bands form the band edges with different energies, one of which lies at the energy shown with the blue (lower-energy) dotted arrow and the other of which lies at the valence-band top in Fig. 2(a). While the energy difference between these band edges are small when calculated without SOC as shown in Fig. 2(b), SOC enhances the hybridization between the Bi- $p_{x,y}$ orbitals, and then the energy difference increases as shown in Fig. 2(a), in the same manner as LaOBiS_2 ¹⁴.

Here, we point out that each band dispersion near the Fermi energy exhibits nearly two-fold degeneracy without the spin degrees of freedom, because there are two BiS_2 layers and two PbS planes in the unit cell of $\text{LaO}(\text{PbS})\text{BiS}_2$ (see Fig. 1). Because these two BiS_2 layers are separated by the rock-salt layer, the band splitting caused by the bilayer coupling between the BiS_2 layers is almost absent for the Bi- p bands. As for LaOBiS_2 , where the BiS_2 layers are neighboring, such a band splitting is actually small, partially by the symmetry of the crystal structure and the Bloch wave functions³⁹, but larger than that in $\text{LaO}(\text{PbS})\text{BiS}_2$.

The last feature of the band structure we mention here is that there is a van Hove singularity (vHs) at the energy of around 0.8 eV indicated by blue solid arrows in Fig. 2(a), which is the same feature as LaOBiS_2 ¹³. We can verify the interesting aspects mentioned above also by looking into DOS shown in Figs. 2(c)–(d). Here, Δ_{vHs} is the energy difference between the vHs indicated by the solid arrows in Figs. 2(a)–(d) and the conduction band bottom.

Figure 2(e) presents the power factor PF, the Seebeck coefficient S , and the electrical conductivity σ , calculated at 300 K with the inclusion of SOC. We can find that the band edges and vHs indicated by the arrows in Fig. 2(c) result in peaks of PF. It

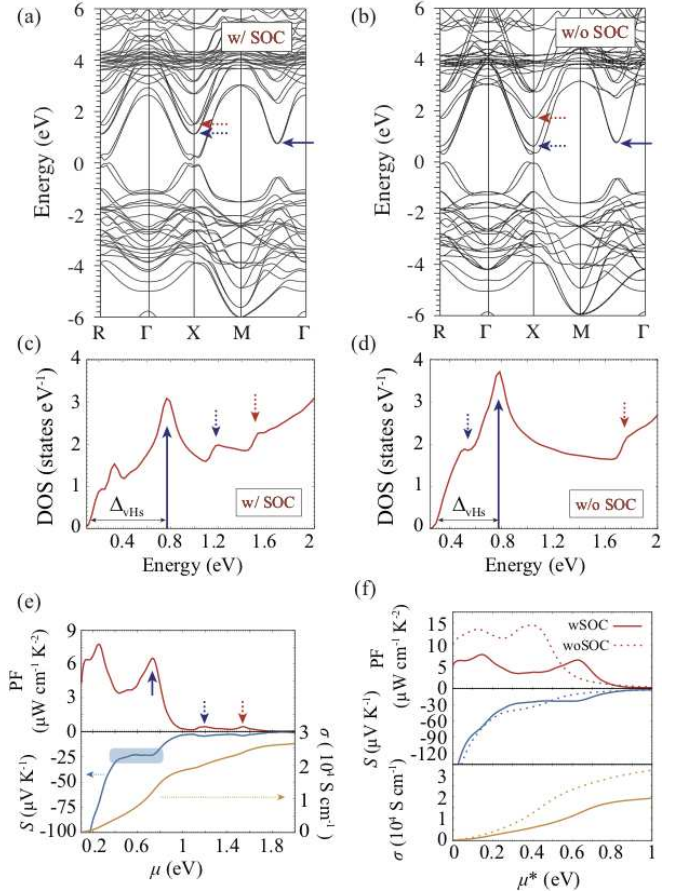


FIG. 2. (a)–(b) First-principles band structure of $\text{LaO}(\text{PbS})\text{BiS}_2$ calculated with and without SOC, respectively. The energy of the valence-band top was set to zero. (c)–(d) DOS of $\text{LaO}(\text{PbS})\text{BiS}_2$ calculated with and without SOC, respectively. The definition of Δ_{vHs} is described in the main text. (e) PF, S , and σ of $\text{LaO}(\text{PbS})\text{BiS}_2$ calculated with SOC at $T = 300$ K. (f) Comparison of the transport properties at $T = 300$ K calculated with and without SOC. The definition of μ^* is described in the main text.

is interesting that the PF peak around $\mu = 0.7$ eV has a comparable height to the PF peak near the conduction band bottom, even though the former is energetically far away from the conduction band bottom. As a matter of fact, the band edges at the X point with higher energies indicated by dotted arrows in Fig. 2(a) cannot yield a large PF peak as shown in Fig. 2(e), because the Seebeck coefficient becomes too small by such a heavy electron doping. The PF peak around $\mu = 0.7$ eV owes to the large DOS of vHs, which prevents the Seebeck coefficient from decreasing by increasing the chemical potential, and also augments the electrical conductivity. If this vHs gets close to the conduction band bottom, i.e., Δ_{vHs} becomes small, the thermoelectric performance is expected to be much improved. As pointed out in Ref.¹⁴, the reduction of Δ_{vHs} is closely related to the enhancement of the quasi-one-dimensionality of the electronic structure. In fact, the conduction band shown in Fig. 2(a) has a sharp dispersion along the Γ -X-M line, but a small Δ_{vHs} corresponds to a less-dispersive nature of the band dispersion along certain directions (concretely, from X to the

center of the Γ -M line). Moreover, the insulating layer makes the band dispersion along the k_z direction nearly flat. Therefore, the band dispersion hosts a quasi-one-dimensionality. In real space, such a quasi-one-dimensionality can be interpreted as a manifestation of the anisotropy of the in-plane Bi and S- p orbitals, which form the square lattice in the BiS₂ conducting layer, similarly to LaOBiS₂¹³. It is advantageous for high thermoelectric performance that such a quasi-one-dimensional band dispersion is degenerate with respect to the spin degrees of freedom and nearly degenerate with respect to the bilayer degrees of freedom. In addition, the equivalency between the x and y directions for the crystal symmetry yields the multi-valley character: one quasi-one-dimensional band is dispersive with respect to the $(k_x + k_y)/\sqrt{2}$ direction and the other for the $(k_x - k_y)/\sqrt{2}$ direction, corresponding to the anisotropy of the $p_{(x\pm y)/\sqrt{2}}$ orbitals along the Bi-S bonds¹³.

It is noteworthy that decreasing Δ_{vHs} (i.e., enhancing the low-dimensionality) was theoretically verified to be a good strategy for enhancing the power factor in LaOPnCh₂¹⁴. One strategy for reducing Δ_{vHs} in LaOPnCh₂ shown in that study is to decrease SOC, which seems to work well also for our system. Figure 2(f) presents the transport properties of LaO(PbS)BiS₂ calculated with and without SOC, where μ^* is defined as the chemical potential measured from the conduction band bottom. For metallic systems we shall investigate later in this paper, μ^* is the Fermi energy, which is set at zero, and so $\mu^* = \mu$ holds. As shown in Fig. 2(f), the electrical conductivity increases by turning off SOC, while keeping the Seebeck coefficient, which results in a sizable enhancement of PF. While the vHs is still far away from the conduction-band bottom even without SOC, an approach of the vHs to the band edge enhances DOS near the band edge as shown in Fig. 2(d). The change of the electronic structure here owes to the suppression of the splitting of the Pn - $p_{x,y}$ bands near the X point. Namely, the small splitting of the Pn - $p_{x,y}$ bands near the X point makes the energy difference between the vHs and the conduction band bottom, Δ_{vHs} , smaller¹⁴. We shall see later that the choice of the Pn atom in LaO(*TtCh*^A)*PnCh*₂^B indeed affects its thermoelectric performance.

We note that the present calculation result shows higher thermoelectric performance than those of experimental previous studies, e.g., PF $\sim 1.5 \mu\text{W cm}^{-1} \text{K}^{-2}$ at 770 K²³, $\sim 0.34 \mu\text{W cm}^{-1} \text{K}^{-2}$ at 300 K²¹. In these experimental studies, the material has been synthesized as polycrystals, so that the thermoelectric efficiency is suppressed due to the presence of insulating layers in between the conducting layers. The present study indicates that the thermoelectric performance of this material can be enhanced if single crystals can be synthesized.

B. Elemental substitution

To seek the possibility of enhancing the thermoelectric performance of LaO(PbS)BiS₂, we have theoretically investigated 24 kinds of materials with the chemical composition LaO(*TtCh*^A)*PnCh*₂^B ($Pn = \text{As, Sb, Bi}$; $Tt = \text{Sn, Pb}$; $Ch^{\text{A,B}} = \text{S, Se}$), which are analogous compounds of LaO(PbS)BiS₂.

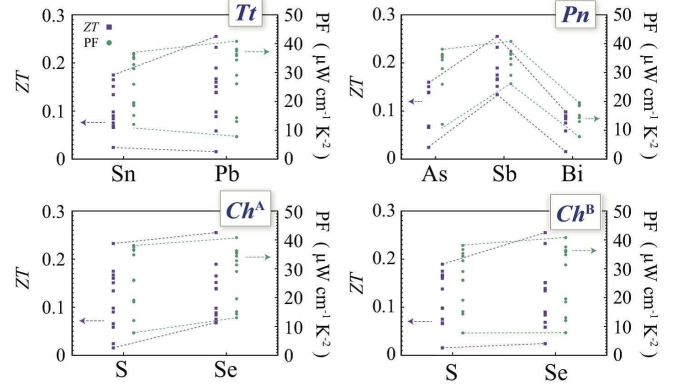


FIG. 3. ZT and PF values of LaO(*TtCh*^A)*PnCh*₂^B calculated at $T = 300 \text{ K}$ using $\kappa_{\text{ph}} = 3.0 \text{ W m}^{-1} \text{K}^{-1}$ and $\tau = 5 \times 10^{-14} \text{ s}$. In each plot, we classified 24 materials with *Tt*, *Pn*, *Ch*^A, and *Ch*^B elements. The dashed lines connect the points with the lowest or highest ZT or PF.

Using $\tau = 5 \times 10^{-15} \text{ s}$ and $\kappa_{\text{ph}} = 3.0 \text{ W m}^{-1} \text{K}^{-1}$, we calculated ZT and PF for these 24 compositions as presented in Fig. 3. In Fig. 3, we can find some trends for PF and ZT with respect to constituent elements: for example, ZT becomes higher for $Tt = \text{Pb}$, $Pn = \text{Sb}$, and $Ch^{\text{A,B}} = \text{Se}$. In fact, we find that LaO(PbSe)SbSe₂ exhibits the highest thermoelectric performance in these candidate materials: PF $\sim 40 \mu\text{W cm}^{-1} \text{K}^{-2}$ and ZT ~ 0.28 for $T = 300 \text{ K}$. From the next section, we shall see the microscopic origin of these trends in detail. We note that these trends remain unaffected also when using $\tau = 10^{-14} \text{ s}$, which we have checked since the relaxation time (to be more precise, the ratio $\tau\kappa_{\text{ph}}^{-1}$) is regarded as an unknown parameter in this study.

1. *Tt* series

To investigate the role of the *Tt* element in the thermoelectric performance, we calculated the electronic band structure of LaO(SnS)BiS₂ as shown in Fig. 4(a). By comparing it with that

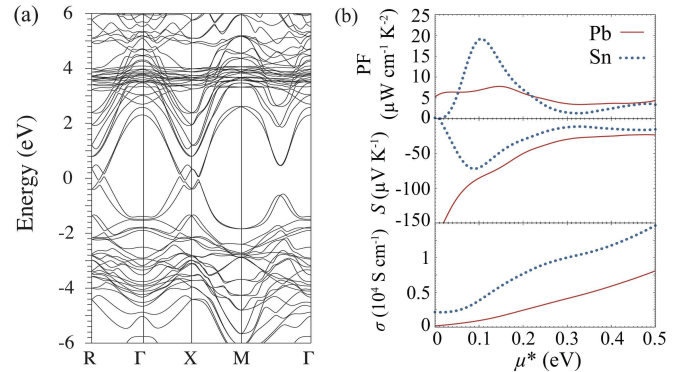


FIG. 4. (a) Electronic band structure of LaO(SnS)BiS₂. (b) σ , S , PF, and (c) ZT of LaO(*Tt*S)BiS₂ for $Tt = \text{Pb}$ and Sn calculated at $T = 300 \text{ K}$.

of $\text{LaO}(\text{PbS})\text{BiS}_2$ shown in Fig. 2(a), a crucial consequence by substituting Pb with Sn is the closing of the band gap. One possible cause of the gap closing is the weakened coupling between the $TtCh^A$ and $PnCh_2^B$ layers for $Tt = \text{Sn}$. In fact, the $Pn-Ch^A$ distance becomes longer by substituting Pb with Sn as listed on Table I in Appendix B. Because the downward and upward convex bands around the Fermi energy mainly consist of the Pn - and Ch^A - p orbitals, respectively²², a long $Pn-Ch^A$ distance for $Tt = \text{Sn}$ will result in a smaller hybridization between these bands around the X point, and hence yield the metallic band structure. We note that all the compositions with $Tt = \text{Sn}$ investigated in this study exhibit a metallic band structure in our calculation, while some compositions with $Tt = \text{Pb}$ have a gapped one, as shown in Table I.

Fig. 4(b) present σ , S and PF of $\text{LaO}(Tt\text{S})\text{BiS}_2$ with $Tt = \text{Sn}$ and Pb. At $\mu^* \approx 0$, the metallic band structure for $Tt = \text{Sn}$ yields a small Seebeck coefficient, which drastically degrades PF. Although PF of $Tt = \text{Sn}$ becomes much higher than $Tt = \text{Pb}$ at $\mu^* \approx 0.1$ eV because of the high electrical conductivity for the former, the merit in ZT is limited because the high electrical conductivity inevitably results in a high electronic thermal conductivity (κ_{el}), which appears in the denominator of ZT . While $\text{LaO}(\text{SnS})\text{BiS}_2$ exhibits a maximum ZT value larger than that of $\text{LaO}(\text{PbS})\text{BiS}_2$, most of the $Tt = \text{Sn}$ group materials have smaller ZT than the materials in the $Tt = \text{Pb}$ group, as shown in Table I. The origin of this trend can be understood by the metallic band structure for $Tt = \text{Sn}$.

2. Pn series

As we have seen in Fig. 3, a remarkable correlation exists between the Pn element and the thermoelectric performance. Based on our observation described in the following analysis, there are two important ingredients that yield this correlation: quasi-one-dimensionality becomes strong by replacing Bi with lighter pnictogen atoms, but the arsenic makes the band structure metallic, which degrades, especially, ZT .

Figures 5(a)–(b) present the electronic band structure of $\text{LaO}(\text{PbS})\text{AsS}_2$ and $\text{LaO}(\text{PbS})\text{SbS}_2$, respectively. The overall characteristics of the band structure are common to $\text{LaO}(\text{PbS})PnS_2$ ($Pn = \text{As, Sb, Bi}$), but one important difference is the gap closing for $Pn = \text{As}$. As a result, the transport properties, σ , S , and PF, of $\text{LaO}(\text{PbS})\text{AsS}_2$ shown in Fig. 5(c) exhibit a behavior similar to those of $\text{LaO}(\text{SnS})\text{BiS}_2$, which we have seen in the previous section. Namely, S and PF become small at $\mu^* \approx 0$ for $\text{LaO}(\text{PbS})\text{AsS}_2$ because of its metallic band structure. Although PF becomes large by heavy carrier doping there, ZT peak is smaller than that of $Pn = \text{Sb}$, as shown in Fig. 5(d), which is likely be due to the large electronic thermal conductivity for $Pn = \text{As}$ with the metallic electronic structure. We note that all the other compositions with $Pn = \text{As}$ also have a metallic band structure as shown in Table I.

For $Pn = \text{Sb}$, where the gap closing does not take place, PF and ZT are much larger than those for $Pn = \text{Bi}$ as shown in Figs. 5(c)–(d). For LaOBiS_2 , some of the present authors pointed out that a quasi-one-dimensionality of the electronic

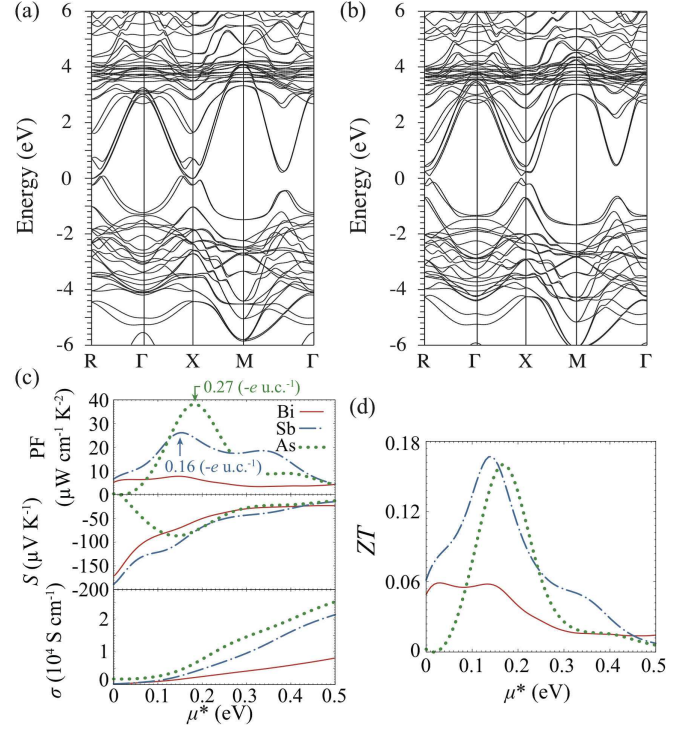


FIG. 5. Electronic band structure of (a) $\text{LaO}(\text{PbS})\text{AsS}_2$ and (b) $\text{LaO}(\text{PbS})\text{SbS}_2$. (c) σ , S , PF, and (d) ZT of $\text{LaO}(\text{PbS})PnS_2$ for $Pn = \text{As, Sb, and Bi}$ calculated at $T = 300$ K. In panel (c), we show the carrier number per unit cell at the chemical potential where PF is maximized for the case of As and Sb.

structure can be drastically enhanced by replacing Bi with Sb or As, because of the suppressed SOC, smaller inter-pnictogen transfer integrals, and the closer energy levels of the Pn and S atomic orbitals¹⁴. In Sec. III A, we have already seen the effect of SOC on thermoelectric performance through the change in Δ_{VHS} , i.e., the quasi-one-dimensionality, for our target material $\text{LaO}(\text{PbS})\text{BiS}_2$. Because both $\text{LaO}(\text{PbS})\text{BiS}_2$ and LaOBiS_2 have the BiS_2 conducting layer, the same strategy for improving the thermoelectric performance is expected to work well. As a matter of fact, we found that Δ_{VHS} decreases from 0.65 eV for $\text{LaO}(\text{PbS})\text{BiS}_2$ to 0.36 eV for $\text{LaO}(\text{PbS})\text{SbS}_2$. As a result, PF and ZT are enhanced for $Pn = \text{As}$ and Sb compared with $Pn = \text{Bi}$. We note that the enhancement in PF shown in Fig. 5(c) is larger than that induced by switching off SOC in $\text{LaO}(\text{PbS})\text{BiS}_2$ shown in Fig. 2(f). This means that, while the suppression of SOC in $Pn = \text{As}$ or Sb plays some role in enhancing PF, other effects described above should also be important in our material. In addition, an important difference between $\text{LaO}(\text{PbS})PnS_2$ and LaOPnS_2 is the possibility of the gap closing for the former, depending on the coupling between the PnS_2 and PbS layers. This difference results in the metallic band structure and thus the degraded thermoelectric performance for $Pn = \text{As}$ as mentioned in the previous paragraph.

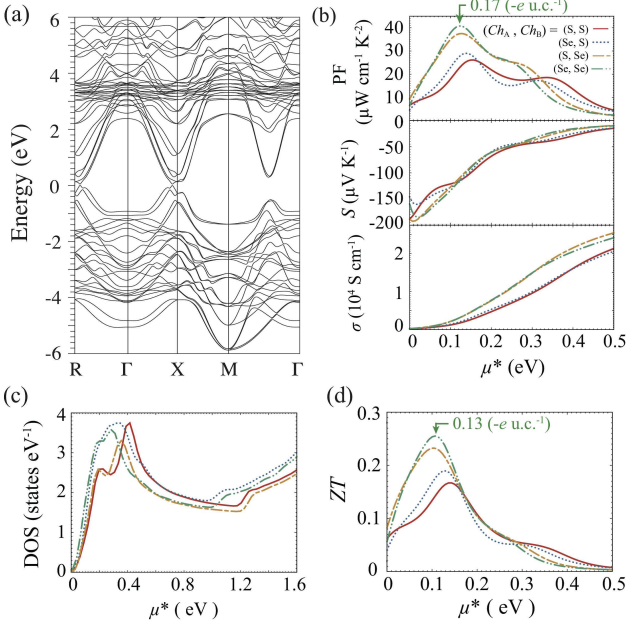


FIG. 6. (a) Electronic band structure of $\text{LaO}(\text{PbSe})\text{SbSe}_2$. (b) σ , S , PF, (c) DOS, and (d) ZT for $\text{LaO}(\text{PbCh}^A)\text{SbCh}_2^B$ ($\text{Ch}^{A,B} = \text{S}, \text{Se}$). Calculation results shown in panels (b) and (d) were obtained using $T = 300$ K. The carrier number per unit cell at the chemical potential where PF or ZT are maximized for $\text{LaO}(\text{PbSe})\text{SbSe}_2$ are shown in panels (b) and (d).

3. Ch series

Figure 6(a) presents the electronic band structure of $\text{LaO}(\text{PbSe})\text{SbSe}_2$. By comparing it with the electronic band structure of $\text{LaO}(\text{PbS})\text{SbS}_2$ shown in Fig. 5(b), we can find that the electronic band structure is less affected by the choice of the Ch atom, except that the valence band structure is slightly shifted upward in Fig. 6(a) because the energy levels of the Se atomic orbitals are higher than those of the S atomic orbitals.

However, by changing Ch^B from S to Se, PF and ZT are sizably enhanced. The calculated values of σ , S , PF, DOS, and ZT for $\text{LaO}(\text{PbCh}^A)\text{SbCh}_2^B$ ($\text{Ch}^{A,B} = \text{S}, \text{Se}$) are shown in Figs. 6(b)–(d). These quantities except of DOS were calculated at $T = 300$ K. By looking into Fig. 6(c), DOS is less affected by Ch^B , but the electrical conductivity shown in Fig. 6(b) exhibits a sizable increase by the change of $Ch^B = \text{S} \rightarrow \text{Se}$, which means that the group velocity is enhanced by this change. A possible reason for it is the approaching energy levels of the $\text{Sb-}p$ orbitals and Ch^B - p orbitals as discussed in Ref.¹⁴ for LaOPnCh_2 , which strengthens the coupling between these atomic orbitals and then sharpens the band dispersion. Consequently, PF reaches a maximum value of nearly $40 \mu\text{W cm}^{-1} \text{K}^{-2}$. This value is similar to that of Bi_2Te_3 , which is well known as a good thermoelectric material at room temperature. Although this comparison is based on a certain assumption for the τ value for the present material, the assumed value is still smaller than the known value for Bi_2Te_3 .

On the other hand, the change of $Ch^A = \text{S} \rightarrow \text{Se}$ only brings a small enhancement of PF and ZT as shown in Figs. 6(b) and

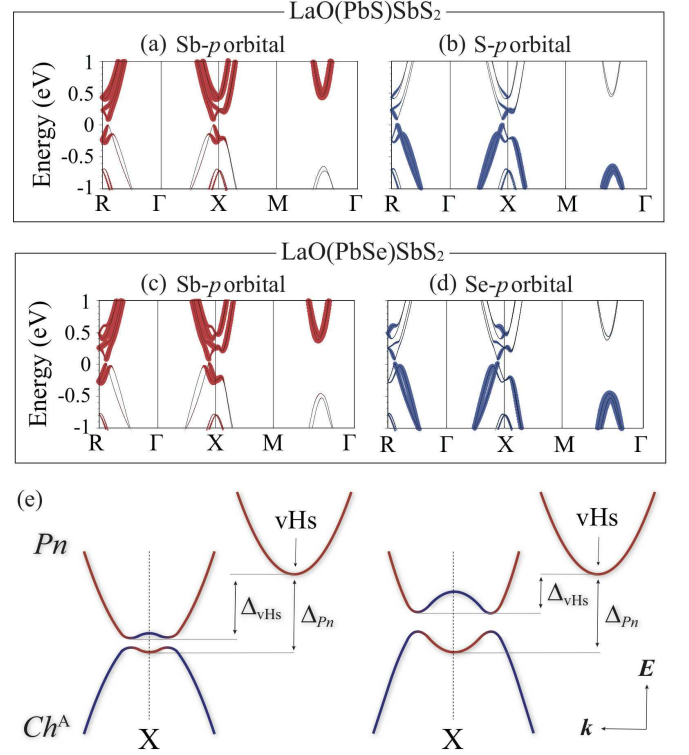


FIG. 7. (a)–(b) The electronic band structure of $\text{LaO}(\text{PbS})\text{SbS}_2$. The colored thickness of the lines indicates the weight of $\text{Sb}(\text{S}_{\text{rock-salt}})\text{-}p$ orbital character. (c)–(d) The same plot for $\text{LaO}(\text{PbSe})\text{SbS}_2$. (e) Schematic figure presenting the hybridization between Pn and Ch^A .

(d). This weak enhancement may come from the increased DOS as shown in Fig. 6(c). To investigate the origin of the DOS enhancement, we employed the Wannier orbitals to show the orbital character onto the band dispersion as presented in Figs. 7(a)–(d). We find that Δ_{vHs} becomes small by the change of $Ch^A = \text{S} \rightarrow \text{Se}$, from 0.30 to 0.37 eV. The situation is schematically shown in Fig. 7(e). Because of the different energy levels for the S- and Se- p orbitals, the Pn band bottom becomes a little far away from the conduction band bottom in $Ch^A = \text{Se}$, as a consequence of the band hybridization shown here. Thus, Δ_{vHs} , which is the energy difference between the conduction band bottom and vHs , becomes smaller in $Ch^A = \text{Se}$. This means the quasi-one-dimensionality is enhanced, which enhances DOS near the band edge.

For all the pairs of $(\text{Ch}^A, \text{Ch}^B)$ for $\text{LaO}(\text{PbCh}^A)\text{SbCh}_2^B$, we verified that the band gap remains opened (see Table I) and the characteristic band deformation as shown in Fig. 7(e) takes place at the X point. Such a deformed band dispersion reminds us of the pudding-mold-shaped band structure⁴⁰, which improves PF through the coexisting large DOS and the large group velocity for several materials^{40–44}.

We note that the effect of the chalcogen atoms on the thermoelectric performance depends on the Tt and Pn elements as shown in Table I. In fact, the correlation between the thermoelectric performance, PF and ZT , and Ch elements is not so strong as shown in Fig. 3. However, this weak correlation

might be natural because of the relatively small difference of the band structure near the Fermi level induced by the chalcogen atoms, as we have seen in this section.

4. The effect of inserting rock-salt layer

In this section, we focus on the effect of inserting rock-salt layer on thermoelectric performance. For this purpose, we calculated the electronic band structure and the thermoelectric properties by using two types of tight-binding models: one consists of all Wannier functions and the other consists of Wannier functions except for those in the rock-salt layer (the $Tt-p$ and the Ch^A-p orbitals). Figures 8 (a)–(b) present the electronic band structures of two types of tight-binding model for $\text{LaO}(\text{PbSe})\text{SbSe}_2$, and those on the $k_z = 0$ plane are shown in Figs. 8 (c)–(d). In Fig. 8 (b), band dispersions originating from the rock-salt layer are not present because we used the tight-binding model not including Wannier functions in the rock-salt layer. On the other hand, in Figs. 8 (a), the band edge near the X point becomes less dispersive and Δ_{vHs} decreases because of the hybridization between the $Pn-p$ and the Ch^A-p bands as discussed in Sec.III A. As shown in Figs. 8 (c)–(d), the band edge near the X point becomes like pudding-mold-shaped band structure (flattened band bottom)

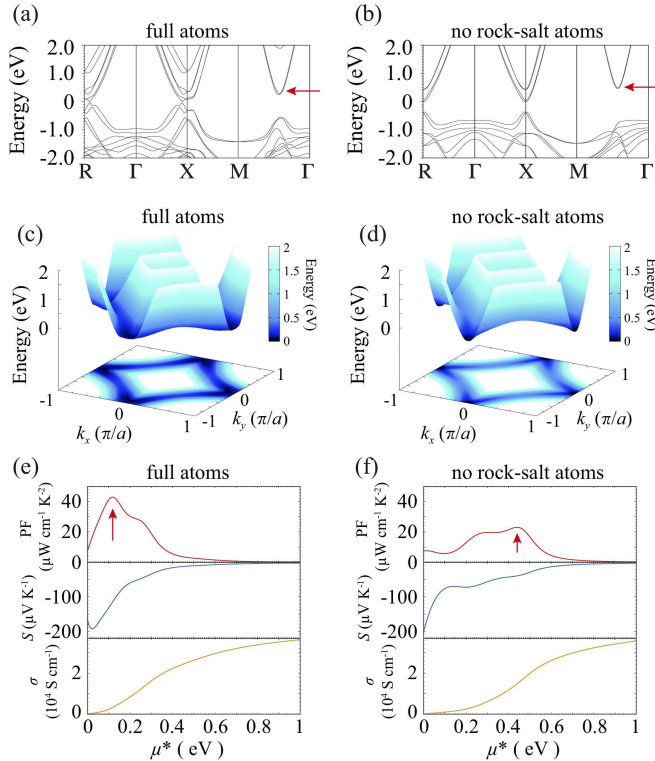


FIG. 8. (a)–(b) Electronic band structures of two types of tight-binding model for $\text{LaO}(\text{PbSe})\text{SbSe}_2$ and (c)–(d) those on the $k_z = 0$ plane colored by the energy value. In panels (a)–(d), the energy of the conduction band bottom was set to zero. (e)–(f) Thermoelectric properties for these models.

and the band dispersion along the lines $|k_x| + |k_y| = \pi$ becomes less dispersive (i.e. quasi-one-dimensionality is enhanced) by inserting the rock-salt layer. The comparison of the thermoelectric properties between two types of tight-binding models is presented in Figs.8 (e)–(f) for $\text{LaO}(\text{PbSe})\text{SbSe}_2$. In the case of $\text{LaO}(\text{PbSe})\text{SbSe}_2$, Δ_{vHs} changes from 0.46 eV to 0.25 eV by inserting rock-salt layer, which results in a PF peak shift as shown with arrows in Figs. 8 (e)–(f). As a consequence of this PF peak shift, the maximum value of PF peak sizably increases by realizing both high Seebeck coefficient and high electrical conductivity. By inserting the rock-salt layer, the proportion of the volume of the conduction layer to the entire bulk is reduced, so that a reduction in the thermoelectric performance should be originally expected. However, it is surprising that there is instead an enhancement of PF. On the other hand, in the case of $\text{LaO}(\text{PbS})\text{BiS}_2$ (shown in appendix B), although Δ_{vHs} becomes small by intercalating rock-salt layer (from 0.81 eV to 0.65 eV), vHs is still far away from conduction band bottom because of the effect of Pn , which we discussed in the Sec.III B 2. Seebeck coefficient becomes too small by such a heavy electron doping and hence PF is also suppressed.

5. Temperature dependence of ZT

Because of the narrow (or even zero) band gap in our target materials, the temperature dependence of the thermoelectric performance is worth investigating. Figure 9 presents the temperature dependence of ZT for $\text{LaO}(\text{PbSe})\text{SbSe}_2$, which exhibits the highest ZT within our calculation shown in this study. Here, the chemical potential is chosen at each temperature so as to realize the maximum ZT at that temperature. We have tried three values for the relaxation time: $\tau = 1, 5, 10$ fs here, which is expected to cover a typical range of the relaxation time in thermoelectric materials. Normally, narrow-gap semiconductor, like this material, cannot exhibit high thermoelectric performance at high temperature, because both electrons and holes are excited, which reduces the See-

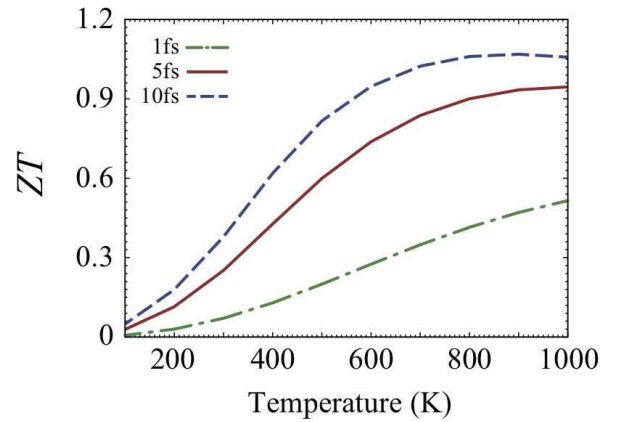


FIG. 9. Temperature dependence of ZT for $\text{LaO}(\text{PbSe})\text{SbSe}_2$ calculated using several values of the relaxation time τ . Here, the chemical potential is chosen at each temperature so as to realize the maximum ZT at that temperature.

beck coefficient (bipolar effect). However, we found that high thermoelectric performance is realized at relatively high temperature in $\text{LaO}(\text{PbSe})\text{SbSe}_2$: ZT reaches around 0.9 at 1000 K for $\tau = 5$ fs, and 1.1 at 900 K for $\tau = 10$ fs. Such a large ZT owes to the deep chemical potential μ^* at the ZT peak as shown in Fig. 6(d), which prevents the generation of the hole carriers. We note that, in reality, the heavy carrier doping and high temperature inevitably shorten the relaxation time through active electron-phonon scattering, which will somewhat suppress ZT at deep μ^* and high temperature. Since the first-principles treatment of the electron-phonon scattering is challenging, this point is an important future issue.

IV. CONCLUSION

We have theoretically investigated the thermoelectric performance (PF and ZT) of $\text{LaO}(\text{TiCh}^{\text{A}})\text{PnCh}_2^{\text{B}}$, and found that $\text{LaO}(\text{PbSe})\text{SbSe}_2$ achieves the best performance among these 24 candidate materials. For $\text{LaO}(\text{PbSe})\text{SbSe}_2$, ZT reaches around 0.9 at 1000 K for $\tau = 5$ fs, and 1.1 at 900 K for $\tau = 10$ fs. This high performance originates from the quasi-one-dimensionality of the electronic structure, which can be enhanced mainly by changing the Pn atom, in the same manner as LaOBiS_2 . The non-zero band gap is also an important factor for high thermoelectric performance. For example, $\text{Ti} = \text{Sn}$ is not favorable for achieving high ZT because of the gap closing, induced by the suppressed coupling between the TiCh^{A} rock-salt layer and the PnCh_2^{B} conducting layer. Hybridization between the PnCh^{A} and TiCh_2^{B} layers is important not

only for opening the gap, but also for making the van Hove singularity closer to the band edge, i.e., for enhancing the low-dimensionality and thus DOS near the band edge. Our study offers a possible designing principle for improving the thermoelectric performance of $\text{LaO}(\text{PbS})\text{BiS}_2$.

ACKNOWLEDGMENTS

We thank Yosuke Goto and Yoshikazu Mizuguchi for fruitful discussion. This work was supported by JST-CREST Grant Number JPMJCR16Q6 and JSPS KAKENHI Grant Numbers JP17H05481, JP17K14108, JP18K13470, JP19H04697.

Appendix A: The effect of inserting rock-salt layer

Electronic band structures and thermoelectric properties of two types of tight-binding models for $\text{LaO}(\text{PbS})\text{BiS}_2$ are shown in Fig. 10.

Appendix B: List of the optimized structural parameters, ZT , PF, and the band gap

Calculated values of the optimized structural parameters, the maximum ZT , the maximum PF, and the band gap of all the materials investigated in this study is shown in Table I.

-
- ¹ Y. Pei, X. Shi, A. LaLonde, H. Wang, L. Chen, and G. J. Snyder, *Nature* **473**, 66 (2011).
 - ² L. D. Hicks and M. S. Dresselhaus, *Phys. Rev. B* **47**, 16631 (1993).
 - ³ H. Usui and K. Kuroki, *J. Appl. Phys.* **121**, 165101 (2017).
 - ⁴ L. D. Hicks and M. S. Dresselhaus, *Phys. Rev. B* **47**, 12727 (1993).
 - ⁵ T. Yamamoto and H. Fukuyama, *J. Phys. Soc. Jpn.* **87**, 114710 (2018).
 - ⁶ Y. Mizuguchi, *J. Phys. Soc. Jpn.* **88**, 041001 (2019).
 - ⁷ Y. Mizuguchi, S. Demura, K. Deguchi, Y. Takano, H. Fujihisa, Y. Gotoh, H. Izawa, and O. Miura, *J. Phys. Soc. Jpn.* **81**, 114725 (2012).
 - ⁸ Y. Mizuguchi, H. Fujihisa, Y. Gotoh, K. Suzuki, H. Usui, K. Kuroki, S. Demura, Y. Takano, H. Izawa, and O. Miura, *Phys. Rev. B* **86**, 220510 (2012).
 - ⁹ Y. Mizuguchi, *J. Phys. Chem. Solids* **84**, 34 (2015).
 - ¹⁰ D. Yazici, I. Jeon, B. White, and M. Maple, *Physica C: Superconductivity and its Applications* **514**, 218 (2015).
 - ¹¹ H. Usui and K. Kuroki, *Novel. Supercond. Mater.* **1**, 50 (2015).
 - ¹² Y. Mizuguchi, A. Nishida, A. Omachi, and O. Miura, *Cogent Physics* **3** (2016).
 - ¹³ H. Usui, K. Suzuki, and K. Kuroki, *Phys. Rev. B* **86**, 220501(R) (2012).
 - ¹⁴ M. Ochi, H. Usui, and K. Kuroki, *Phys. Rev. Applied* **8**, 064020 (2017).
 - ¹⁵ M. Ochi, H. Usui, and K. Kuroki, *J. Phys. Soc. Jpn.* **88**, 041010 (2019).
 - ¹⁶ C. H. Lee, A. Nishida, T. Hasegawa, H. Nishiate, H. Kunioka, S. Ohira-Kawamura, M. Nakamura, K. Nakajima, and Y. Mizuguchi, *Appl. Phys. Lett.* **112**, 023903 (2018).
 - ¹⁷ C.-H. Lee, *J. Phys. Soc. Jpn.* **88**, 041009 (2019).
 - ¹⁸ A. Nishida, O. Miura, C.-H. Lee, and Y. Mizuguchi, *Appl. Phys. Express* **8**, 111801 (2015).
 - ¹⁹ Y. Goto, A. Miura, R. Sakagami, Y. Kamihara, C. Moriyoshi, Y. Kuroiwa, and Y. Mizuguchi, *J. Phys. Soc. Jpn.* **87**, 074703 (2018).
 - ²⁰ Y. Goto, A. Miura, C. Moriyoshi, Y. Kuroiwa, and Y. Mizuguchi, *J. Phys. Soc. Jpn.* **88**, 024705 (2019).
 - ²¹ Y.-L. Sun, A. Ablimit, H.-F. Zhai, J.-K. Bao, Z.-T. Tang, X.-B. Wang, N.-L. Wang, C.-M. Feng, and G.-H. Cao, *Inorg. Chem.* **53**, 11125 (2014).
 - ²² Y. Mizuguchi, Y. Hijikata, T. Abe, C. Moriyoshi, Y. Kuroiwa, Y. Goto, A. Miura, S. Lee, S. Torii, T. Kamiyama, C. H. Lee, M. Ochi, and K. Kuroki, *EPL* **119**, 26002 (2017).
 - ²³ Y. Yu, C. Wang, Q. Li, C. Cheng, S. Wang, and C. Zhang, *Ceram. Int.* **45**, 817 (2019).
 - ²⁴ K. Momma and F. Izumi, *J. Appl. Crystallogr* **44**, 1272 (2011).
 - ²⁵ J. P. Perdew, A. Ruzsinszky, G. I. Csonka, O. A. Vydrov, G. E. Scuseria, L. A. Constantin, X. Zhou, and K. Burke, *Phys. Rev. Lett.* **100**, 136406 (2008).
 - ²⁶ G. Kresse and D. Joubert, *Phys. Rev. B* **59**, 1758 (1999).

TABLE I. Calculated values of the optimized structural parameters, the maximum ZT , the maximum PF, and the band gap of all the materials investigated in this study. the maximum ZT and the maximum PF were calculated at 300 K using $\tau = 5.0 \times 10^{-15}$ s and $\kappa_{\text{ph}} = 3.0 \text{ W m}^{-1} \text{ K}^{-1}$.

Tt	Pn	Ch^A	Ch^B	a (Å)	c (Å)	$Pn-Ch^A$ (Å)	ZT	PF ($\mu\text{W cm}^{-1} \text{ K}^{-2}$)	Band gap (eV)
Pb	Bi	S	S	4.06	19.6	3.19	0.06	7.8	0.11
		S	Se	4.13	20.2	3.24	0.06	7.8	0.05
		Se	S	4.11	19.7	3.25	0.10	14.3	0
		Se	Se	4.18	20.3	3.29	0.09	13.0	0
	Sb	S	S	4.03	19.3	3.10	0.17	26.1	0.09
		S	Se	4.09	19.8	3.10	0.23	37.5	0.06
		Se	S	4.08	19.4	3.17	0.19	29.0	0.06
		Se	Se	4.14	20.0	3.17	0.26	40.8	0.04
	As	S	S	3.97	18.7	2.99	0.16	38.1	0
		S	Se	4.02	19.3	2.97	0.15	36.3	0
		Se	S	4.02	18.8	3.12	0.14	34.3	0
		Se	Se	4.07	19.5	3.08	0.14	35.8	0
Sn	Bi	S	S	4.02	19.6	3.24	0.10	19.1	0
		S	Se	4.09	20.5	3.48	0.09	18.5	0
		Se	S	4.07	19.7	3.25	0.08	15.1	0
		Se	Se	4.14	20.4	3.35	0.08	19.6	0
	Sb	S	S	3.99	19.2	3.14	0.17	36.7	0
		S	Se	4.06	19.9	3.21	0.13	34.8	0
		Se	S	4.04	19.3	3.16	0.17	32.7	0
		Se	Se	4.10	20.0	3.20	0.15	36.2	0
	As	S	S	3.91	18.7	2.98	0.07	25.9	0
		S	Se	3.97	19.3	3.03	0.02	12.0	0
		Se	S	3.96	18.9	3.10	0.07	35.3	0
		Se	Se	4.02	19.5	3.11	0.07	31.3	0

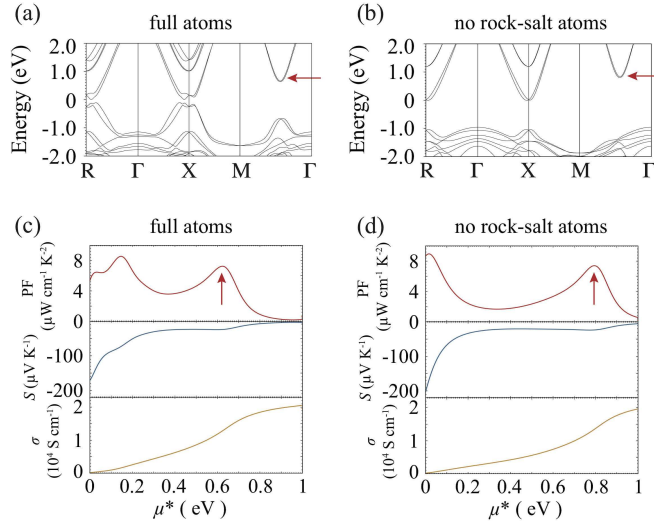


FIG. 10. (a)–(b) Electronic band structures and (c)–(d) thermoelectric properties of two types of tight-binding models for $\text{LaO}(\text{PbS})\text{BiS}_2$. In panels (a)–(b), the energy of the conduction band bottom was set to zero.

²⁷ G. Kresse and J. Hafner, Phys. Rev. B **47**, 559 (1993).

²⁸ G. Kresse and J. Hafner, Phys. Rev. B **49**, 14251 (1994).

²⁹ G. Kresse and J. Furthmüller, Comput. Mater. Sci. **6**, 15 (1996).

³⁰ G. Kresse and J. Furthmüller, Phys. Rev. B **54**, 11169 (1996).

³¹ A. D. Becke and E. R. Johnson, J. Chem. Phys. **124**, 221101 (2006).

³² F. Tran and P. Blaha, Phys. Rev. Lett. **102**, 226401 (2009).

³³ P. Blaha, K. Schwarz, G. K. H. Madsen, D. Kvasnicka, and J. Luitz, *WIEN2K: An Augmented Plane Wave Plus Local Orbitals Program for Calculating Crystal Properties*, Technische Universität Wien, Vienna, (2001).

³⁴ G. Madsen and D. Singh, Comput. Phys. Commun. **175** (2006).

³⁵ A. A. Mostofi, J. R. Yates, Y.-S. Lee, I. Souza, D. Vanderbilt, and N. Marzari, Comput. Phys. Commun. **178**, 685 (2008).

³⁶ J. Kuneš, R. Arita, P. Wissgott, A. Toschi, H. Ikeda, and K. Held, Comput. Phys. Commun. **181**, 1888 (2010).

³⁷ I. Souza, N. Marzari, and D. Vanderbilt, Phys. Rev. B **65**, 035109 (2001).

³⁸ N. Marzari and D. Vanderbilt, Phys. Rev. B **56**, 12847 (1997).

³⁹ M. Ochi, R. Akashi, and K. Kuroki, J. Phys. Soc. Jpn. **85**, 094705 (2016).

⁴⁰ K. Kuroki and R. Arita, J. Phys. Soc. Jpn. **76**, 083707 (2007).

⁴¹ H. Usui, R. Arita, and K. Kuroki, J. Phys. Condens. Matter **21**, 064223 (2009).

⁴² H. Usui, K. Suzuki, K. Kuroki, S. Nakano, K. Kudo, and M. Nohara, Phys. Rev. B **88**, 075140 (2013).

⁴³ K. Mori, H. Sakakibara, H. Usui, and K. Kuroki, Phys. Rev. B **88**, 075141 (2013).

⁴⁴ H. Usui, K. Kuroki, S. Nakano, K. Kudo, and M. Nohara, J. Electron. Mater. **43**, 1656 (2014).